

**Supplemental Material:**  
**Three-dimensional electronic structure in ferromagnetic  $\text{Fe}_3\text{Sn}_2$**   
**with breathing kagome bilayers**

Hiroaki Tanaka,<sup>1</sup> Yuita Fujisawa,<sup>2</sup> Kenta Kuroda,<sup>1,\*</sup> Ryo Noguchi,<sup>1</sup> Shunsuke Sakuragi,<sup>1</sup> Cédric Bareille,<sup>1</sup> Barnaby Smith,<sup>2</sup> Cephise Cacho,<sup>3</sup> Sung Won Jung,<sup>3</sup> Takayuki Muro,<sup>4</sup> Yoshinori Okada,<sup>2</sup> and Takeshi Kondo<sup>1,5,†</sup>

<sup>1</sup>*ISSP, University of Tokyo, Kashiwa, Chiba 277-8581, Japan*

<sup>2</sup>*Okinawa Institute of Science and Technology*

*Graduate University, Okinawa 904-0495, Japan*

<sup>3</sup>*Diamond Light Source, Harwell Campus,*

*Didcot OX11 0DE, United Kingdom*

<sup>4</sup>*Japan Synchrotron Radiation Research Institute (JASRI),*

*1-1-1 Kouto, Sayo, Hyogo 679-5198, Japan*

<sup>5</sup>*Trans-scale Quantum Science Institute,*

*University of Tokyo, Bunkyo-ku, Tokyo 113-0033, Japan*

## Note 1. Tight-binding model and group theoretical analysis of the kagome lattice

In this Note, we discuss the effects of the breathing and spin-orbit coupling (SOC) on the kagome lattice. First, we calculate the band dispersions of the kagome lattice using the tight-binding model in Ref. [24]. After the Fourier transformation of eq. (4) in Ref. [24], we obtain the following  $6 \times 6$  matrix Hamiltonian:

$$\mathcal{H}(\mathbf{k}) = - \begin{pmatrix} 0 & \hat{t}_1^\dagger e^{i\mathbf{k}\cdot\mathbf{a}_1/2} + \hat{t}_1' e^{-i\mathbf{k}\cdot\mathbf{a}_1/2} & \hat{t}_3 e^{-i\mathbf{k}\cdot\mathbf{a}_3/2} + \hat{t}_3' e^{i\mathbf{k}\cdot\mathbf{a}_3/2} \\ \hat{t}_1 e^{-i\mathbf{k}\cdot\mathbf{a}_1/2} + \hat{t}_1' e^{i\mathbf{k}\cdot\mathbf{a}_1/2} & 0 & \hat{t}_2^\dagger e^{i\mathbf{k}\cdot\mathbf{a}_2/2} + \hat{t}_2' e^{-i\mathbf{k}\cdot\mathbf{a}_2/2} \\ \hat{t}_3^\dagger e^{i\mathbf{k}\cdot\mathbf{a}_3} + \hat{t}_3' e^{-i\mathbf{k}\cdot\mathbf{a}_3/2} & \hat{t}_2 e^{-i\mathbf{k}\cdot\mathbf{a}_2/2} + \hat{t}_2' e^{i\mathbf{k}\cdot\mathbf{a}_2/2} & 0 \end{pmatrix} \quad (1)$$

where the vectors  $\mathbf{a}_j$  and the hopping operators  $\hat{t}_j$  and  $\hat{t}_j'$  are defined in the reference ( $j = 1, 2, 3$ ). We introduce new parameters  $\beta = \delta/t_0$  and  $t_{\text{total}} = \sqrt{t_0^2 + \lambda_{0,i}^2 + \lambda_{0,R}^2}$  to simplify the equations, then the hopping operators  $\hat{t}_j$  and  $\hat{t}_j'$  can be represented as follows:

$$\hat{t}_j = (1 + \beta)t_{\text{total}} \exp(i\phi \hat{\mathbf{d}}_j \cdot \boldsymbol{\sigma}), \quad \hat{t}_j' = (1 - \beta)t_{\text{total}} \exp(i\phi \hat{\mathbf{d}}_j \cdot \boldsymbol{\sigma})$$

$\beta$  and  $\phi$  correspond to the strengths of the breathing and SOC, respectively. The band dispersions of several types of kagome lattices are summarized in Fig. S1.

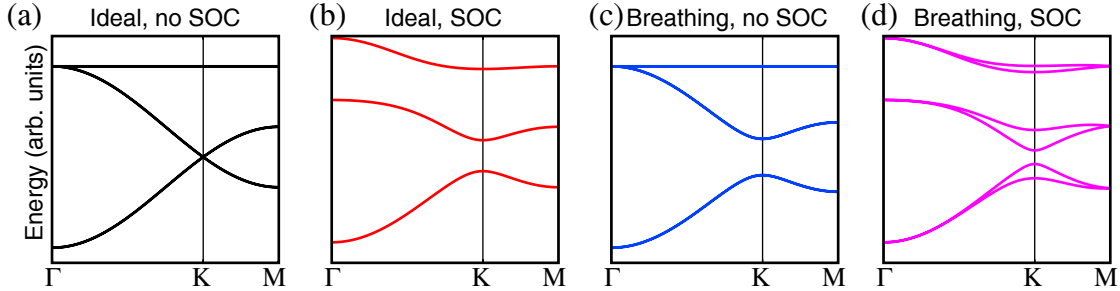


FIG. S1. Calculated band dispersions using the tight-binding model of (a) ideal kagome lattice without SOC, (b) ideal kagome lattice with SOC, (c) breathing kagome lattice without SOC, and (d) breathing kagome lattice with SOC. The breathing parameter  $\beta$  is equal to 0.2 in (c), 0.05 in (d), and 0 otherwise. The SOC parameter  $\phi$  is equal to  $-0.3$  when SOC is on, and 0 otherwise. The SOC angle parameter  $\alpha$  is  $\pi/2$  (intrinsic SOC) in the whole cases.

\* kuroken224@issp.u-tokyo.ac.jp

† kondou1215@issp.u-tokyo.ac.jp

TABLE SI. Irreducible representations of the ideal kagome lattice

Point	Spin Neglected	Spin Included
$\Gamma$ ( $6mm$ )	$A_1 + E_2$	$E_{1/2} + E_{3/2} + E_{5/2}$
K ( $3m$ )	$A_1 + E$	$2E_{1/2} + E_{3/2}$
M ( $2mm$ )	$A_1 + B_1 + B_2$	$3E_{1/2}$

TABLE SII. Irreducible representations of the breathing kagome lattice

Point	Spin Neglected	Spin Included
$\Gamma$ ( $3m$ )	$A_1 + E$	$2E_{1/2} + E_{3/2}$
K ( $3$ )	$A + E$	$2E_{1/2} + 2B_{3/2}$
M ( $m$ )	$2A' + A''$	$3E_{1/2}$

Tables SI and SII show how the degenerations appear and disappear at highly symmetric  $\Gamma$ , K, and M points in the kagome lattice. In the following argument based on Refs. [17, 26-28], we consider two-dimensional point groups. In two dimensions, the ideal kagome lattice has 6-fold rotational symmetry and six mirror planes ( $6mm$ ) and the breathing lattice has 3-fold rotational symmetry and three mirror planes ( $3m$ ). Figures S1(a) and (c) correspond to the spin neglected cases (three eigenstates) and S1(b) and (d) correspond to the spin included cases (six eigenstates). We note that in Fig. S1(b) double degenerations occur anywhere nonetheless with the inclusion of SOC.

We use, as basis functions, wave functions centered at each atom in the kagome unit cell. In the first columns of the tables, the parentheses on the right of each point label enclose the symbol of the point group of the operations which keep the point invariant in the reciprocal space. The characters of the representation of our basis functions are calculated and then the representation is reduced to several irreducible representations as shown in Tables SI and SII.

An irreducible representation  $E$  (sometimes with subscripts) is two-dimensional, which generally means a double degeneration. The exception of the degeneration is the case where  $E$  can be reduced to two one-dimensional irreducible representations in the range of complex numbers and the Kramers degeneration does not occur. Since external field is not applied, time-reversal symmetry (TRS) allows the Kramers degeneration. However, for the additional

degeneration originating from the TRS to occur in band dispersions, the lattice needs to have the space inversion symmetry or the high-symmetric point needs to be one of the time-reversal invariant momenta (TRIM). Since the ideal kagome lattice has the space inversion symmetry and the  $\Gamma$  and M points are TRIM, physically irreducible two-dimensional representations cause degenerations in these situations. The K points in the breathing kagome lattice do not satisfy the above two conditions, and therefore the degeneration does not occur. With these considerations, the appearance and disappearance of the degenerations represented in Fig. S1 can be explained.

## Note 2. Berry curvature of the TRS-breaking kagome lattice

To calculate the Berry curvature, we now break the TRS by some external magnetic field. As a result, only one direction of spin (up spin is used here) is considered. We compose the  $3 \times 3$  Hamiltonian from eq. (1) by extracting the odd lines and the odd columns. In the cases where either one of SOC and the breathing is included, the band dispersions of the  $3 \times 3$  Hamiltonian is the same as Figs. S1(b) or (c). When both are included, the gap sizes at the K and  $K'$  points become different [Fig. S2(a)], where the  $K'$  point is the symmetric position of the K point with respect to the  $\Gamma$  point.

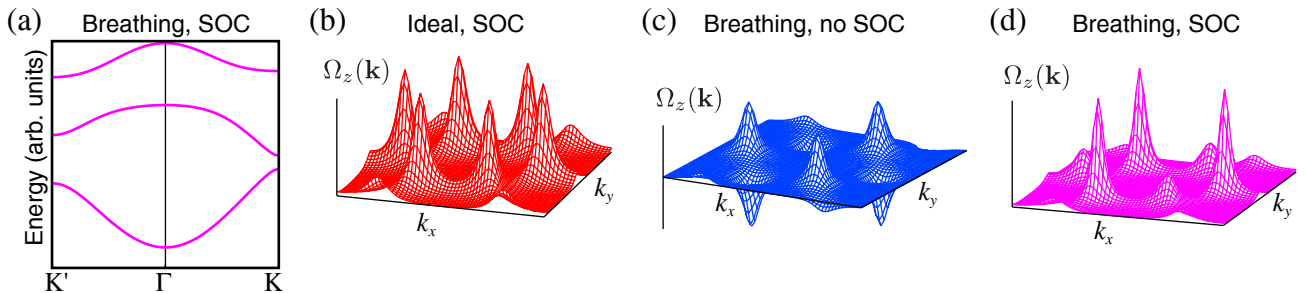


FIG. S2. Berry curvature of the kagome lattice. (a) Band dispersions of the  $3 \times 3$  Hamiltonian with the inclusion of the breathing and SOC. (b) Berry curvature (in arbitrary units) of the ideal kagome lattice with SOC, (c) that of the breathing kagome lattice without SOC, and (d) that of the breathing kagome lattice with SOC. Local maxima or minima are at the K or  $K'$  points.  $\beta$  is set to 0.2 in (c) and 0.05 in (d) and  $\phi$  is set to  $-0.3$  in (b) and (d).

The Berry curvature of the lowest band is calculated according to the definition  $\mathbf{\Omega}(\mathbf{k}) =$

$i(\nabla_{\mathbf{k}}\psi^*(\mathbf{k})) \times (\nabla_{\mathbf{k}}\psi(\mathbf{k}))$  [2], where  $\psi(\mathbf{k})$  is the eigenstate of the lowest band. Figures S2(b), (c), and (d) show the  $z$  components of the Berry curvatures. The Berry curvature caused by SOC is an even function with Chern number 1, while that caused by the breathing is odd with Chern number 0. When both are included, the difference of the gap sizes appears in the magnitude of the Berry curvature.

### Note 3. Group theoretical analysis of the breathing kagome bilayer

We obtain degeneration properties of the breathing kagome bilayer based on group theory. In this Note, we neglect the spin and SOC and calculate the representations with six basis functions of the bilayer lattice, similarly to the previous research about ferromagnetic kagome bilayer [20].

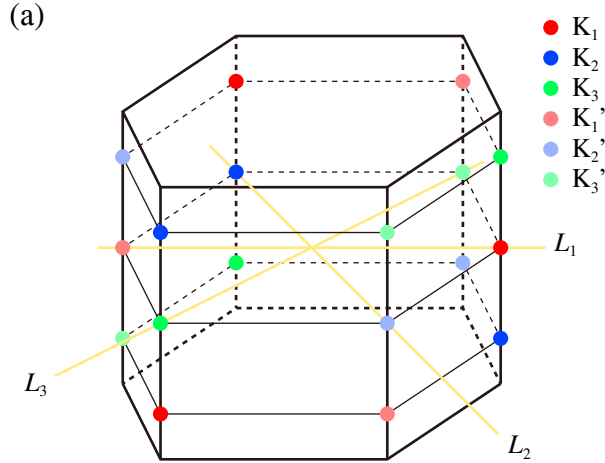


FIG. S3. (a) Distribution of the K points. 2-fold rotational operation along the axis  $L_i$  keeps the  $K_i$  and  $K_i'$  invariant ( $i = 1, 2, 3$ ).

First, we use the primitive rhombohedral unit cell in the real space and the hexagonal column unit cell in the reciprocal space, which corresponds to the periodicity of ARPES spectra. Because of the unusual stacking of the hexagonal column unit cells discussed in the main text, all K points are treated as different (but equivalent) points [Fig. S3]. For example,  $\left(\frac{4\pi}{3a}, 0, 0\right)$ ,  $\left(-\frac{2\pi}{3a}, \frac{2\pi}{\sqrt{3}a}, \frac{2\pi}{c}\right)$ , and  $\left(-\frac{2\pi}{3a}, -\frac{2\pi}{\sqrt{3}a}, -\frac{2\pi}{c}\right)$  are the same points labeled by  $K_1$ . Therefore, the K points are not invariant under 3-fold rotations. In the space group  $R\bar{3}m$ , only a 2-fold rotational operation along an axis on the  $k_x k_y$  plane keeps the K points

TABLE SIII. Irreducible representations of the breathing kagome monolayer and bilayer. Parentheses in the first column encloses the symbols of the space groups of the bilayer.

Point	Monolayer	Bilayer
$\Gamma$ ( $\bar{3}m$ )	$A_1 + E$	$(A_{1g} + A_{2u}) + (E_g + E_u)$
K (32)	$A + E$	$(A_1 + A_2) + 2E$
M ( $2/m$ )	$2A' + A''$	$2(A_g + B_u) + (B_g + A_u)$

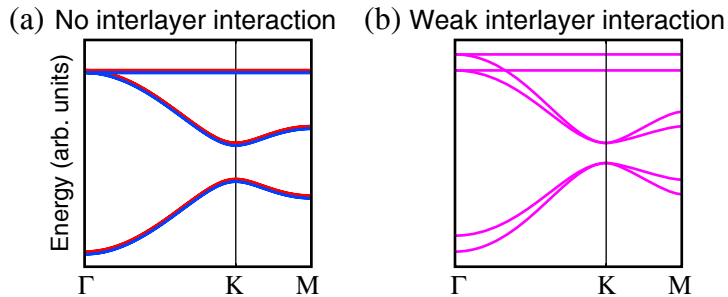


FIG. S4. Schematics of band dispersions of the breathing kagome bilayer when the conventional unit cell is used. (a) Schematic of band dispersions of breathing kagome bilayer with no interlayer interaction and (b) that with weak interaction, keeping degeneration properties obtained from group theoretical analysis. The band crossing between the  $\Gamma$  and K points is not systematic and thus may not exist.

invariant [Fig. S3], then the representation is reduced to  $3A + 3B$  (no degeneration).

If we use the conventional unit cell, the reciprocal unit cell is folded to a hexagonal column with a height of  $2\pi/c$ . The three-dimensional space group of a high-symmetry point includes the two-dimensional space group, so we can extend two-dimensional irreducible representations [Table SII] to three-dimensional ones. Table SIII shows degeneration properties at the  $\Gamma$ , K, and M points. Actually two degenerations occur at the K points, but if we assume weak interlayer interaction, the degenerated bands will be parabolic [Fig. S4(b)]. Therefore, these degenerations do not necessarily mean the vanishment of the breathing effect.

#### Note 4. Sample growth and X-ray diffraction

The samples were grown by chemical vapor transport. Figure S5(a) shows a typical image of an obtained crystal, showing clear plate-like morphology with a hexagonal shape.

The crystals were characterized by X-ray diffraction (XRD) using a Bruker D8 Venture (single crystal) and a Bruker D8 Discover (out of plane). The lattice constants  $a = b = 5.35 \text{ \AA}$  and  $c = 19.82 \text{ \AA}$  were determined based on single crystal XRD data. Figure S5(b) shows the out of plane diffraction ( $00l$ ). There are no secondary crystal phases and all peaks are indexed in accordance with the expected  $\text{Fe}_3\text{Sn}_2$  crystal.

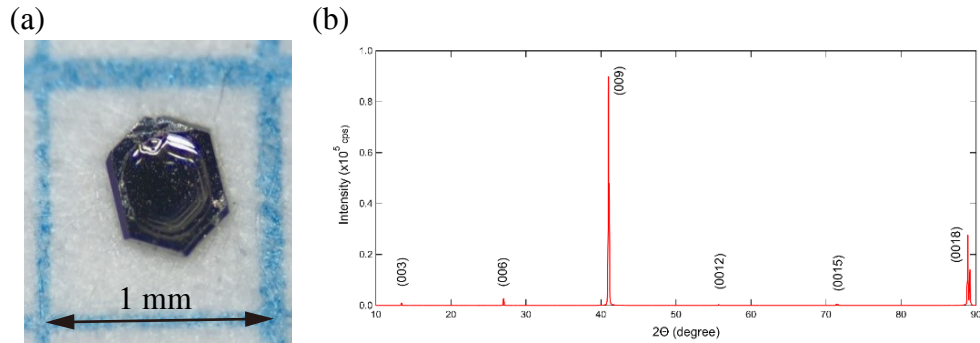


FIG. S5. Growth and characterization of  $\text{Fe}_3\text{Sn}_2$  single crystals. (a) Picture of a typical crystal with a clear hexagonal shape. (b) Out of plane X-ray diffraction pattern with clear ( $00l$ ) peaks.

#### Note 5. Bulk states observed by VUV-ARPES

Figure S6 shows bulk bands observed by VUV-ARPES. In the constant-energy mapping [Fig. S6(a)], dispersions show a long periodicity of the three-dimensional states. Additionally, the triangular-shaped pocket centered at the  $\bar{\Gamma}_1$  point [Fig. S6(b)] reflects 3-fold rotational symmetry and mirror planes originating from the three-dimensionality. The graph of the MDCs with different rotational angles [Fig. S6(c)] shows three cycles of the change of the peak positions in  $2\pi$  rotation, which supports the triangular shape of the pocket.

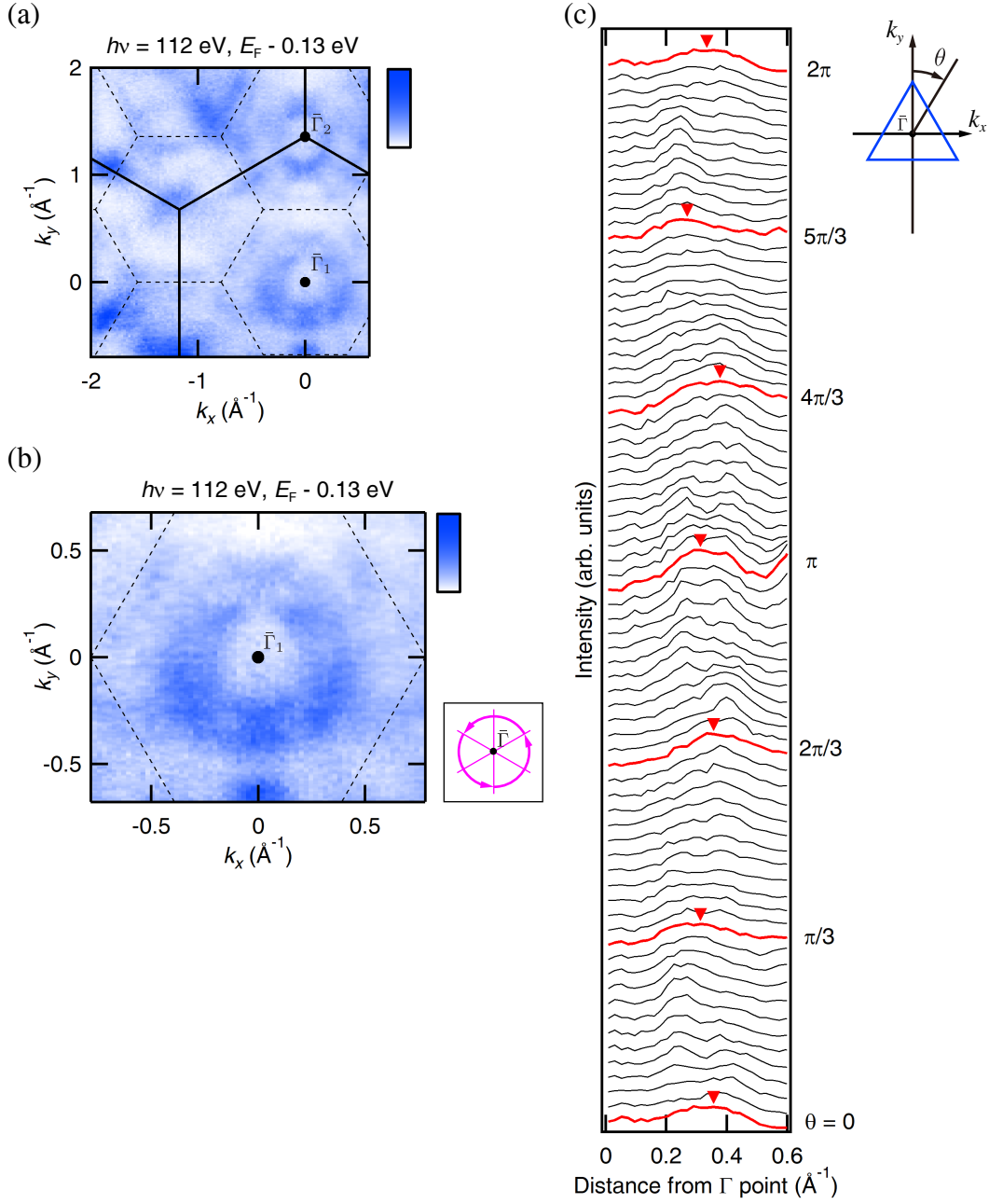


FIG. S6. Bulk states measured by VUV light. (a) Constant-energy mapping measured by 112 eV VUV light. The solid lines are the periodicity of the three-dimensional states and the dashed lines are that of the two-dimensional states. (b) Triangular-shaped pocket centered at the  $\bar{\Gamma}_1$  point. The pink arrow arcs and lines in the bottom right corner represent 3-fold rotational symmetry and three mirror planes of the bulk states. (c) MDCs with different rotational angles  $\theta$ . The schematic in the top right corner shows the definition of  $\theta$ .

### Note 6. Negligible $k_z$ dispersion measured by VUV-ARPES

Figure S7(b) shows momentum distribution curves corresponding to the  $k_y$ - $k_z$  mapping taken by VUV-ARPES [Fig. S7(a)]. Although the matrix element effects weakened the intensity of several peaks, one can see negligible  $k_z$  dispersion along overlaid blue lines.

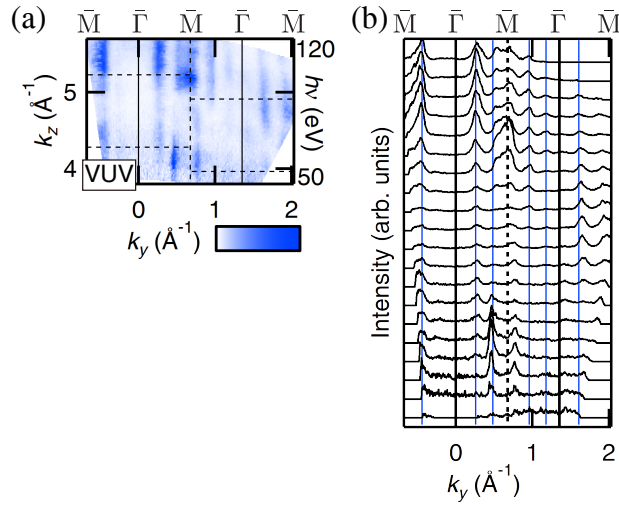


FIG. S7. Negligible  $k_z$  dispersion measured by VUV-ARPES. (a)  $k_y$ - $k_z$  mapping at the Fermi energy measured by VUV light [same as Fig. 3(a)]. (b) Momentum distribution curves of (a), with overlaid vertical blue lines.

## Note 7. Curvature plot of SX-ARPES mapping

We used curvature plot [38], which can enhance several band dispersions, to the SX-ARPES mapping shown in Fig. S8(a). Figure S8(b) shows the enhanced bulk band dispersions.

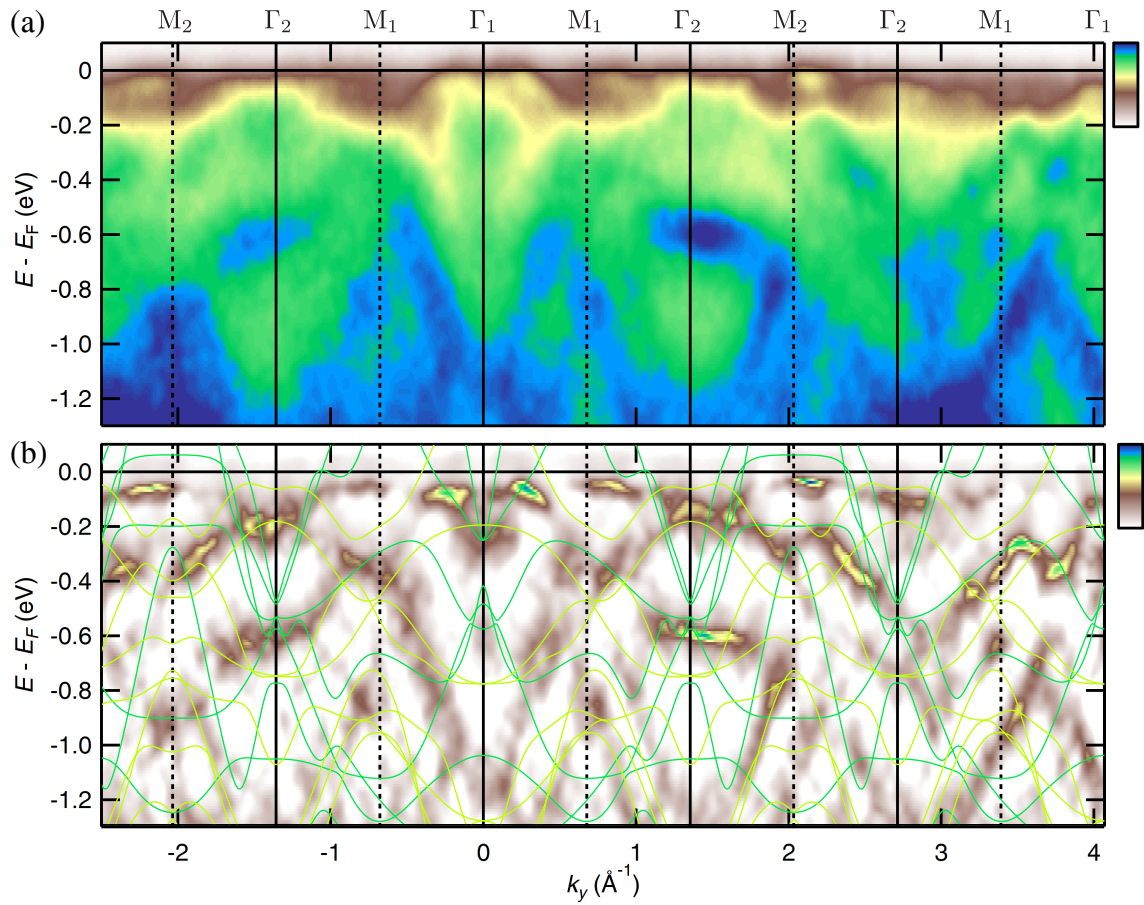


FIG. S8. Enhanced band dispersions by curvature plot. (a) Original SX-ARPES mapping along the  $k_y$  direction [same as Fig. 4(a)]. (b) Curvature plot of (a), with overlaid DFT band dispersions.

### Note 8. DFT band dispersions near $\bar{K}$ point

Figure S9 shows DFT band dispersions near the  $\bar{K}$  point from  $k_z = 0$  (the  $\Gamma$  point is on the plane) to  $k_z = 3\pi/c$  (the Z point is on the plane). The horizontal axes are the same as that of Fig. 4(g) in the main text.

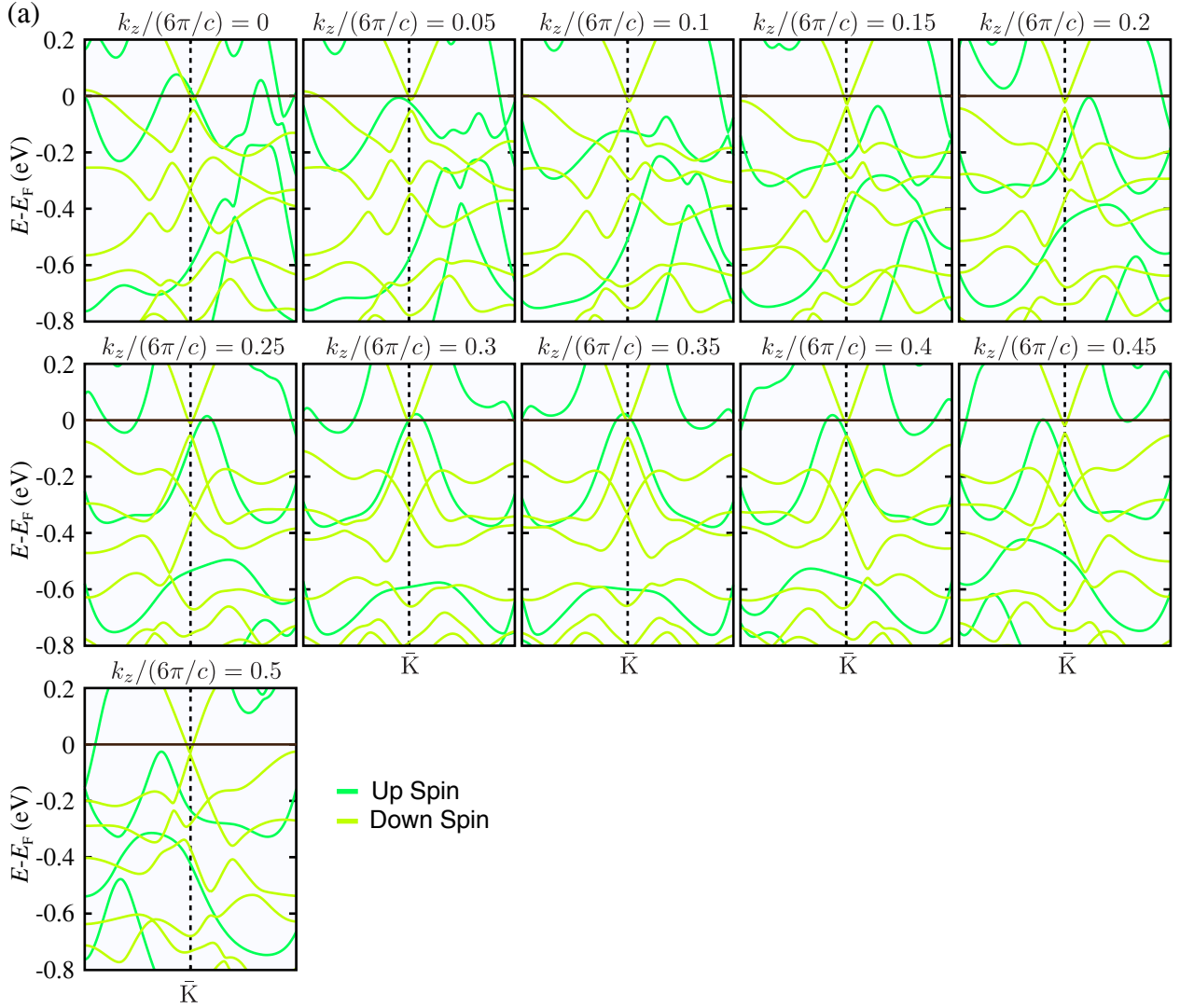


FIG. S9. DFT band dispersions near the  $\bar{K}$  point with the difference of the  $k_z$  coordinate.